

Article pubs.acs.org/acsaelm

Role of the Blend Ratio in Polymer: Fullerene Phototransistors

Cinthya Trujillo Herrera, Min Ji Hong, and John G. Labram*



Cite This: ACS Appl. Electron. Mater. 2020, 2, 2257-2264



ACCESS I

Metrics & More

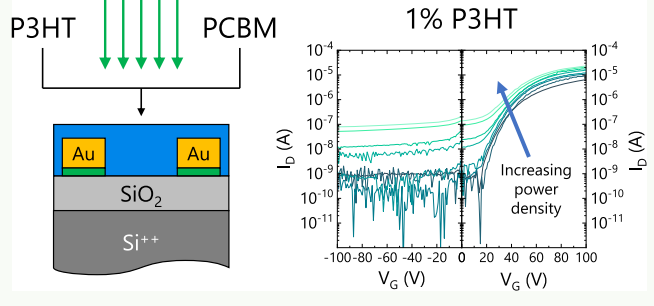


Supporting Information

ABSTRACT: Because of their ability to combine detection and processing into a single element, phototransistors have the potential to be a disruptive optical-detection technology. Unfortunately, however, at present the relationship between current and incident optical power density is complicated and poorly understood. In this report, we investigate how the ratio of polymer to fullerene affects the performance of organic phototransistors. We find the surprising result that even a small percentage (1% by weight) of polymer can modify the optical response of organic phototransistors to green light significantly. Polymer:fullerene phototransistors such as those demonstrated in this report have the combined advantages of being

highly optically transparent to the excitation wavelength and being unipolar.

KEYWORDS: phototransistors, OFETs, organic semiconductors, polymer:fullerene, TRMC



INTRODUCTION

Low-cost, large-area, semiconductors represent a bold vision of the future in which electronics is omnipresent. This vision includes inexpensive, conformal, and stretchable electronics embedded into our natural surroundings.^{2,3} In particular, solution-processable materials such as organic semiconductors, 4 metal oxides, 5 and metal halide perovskites 6 enable lowcost, flexible, optical detectors with a range of physical forms. Although 2-terminal photodiodes have been studied as optical sensors in many applications, 8-11 there are strong arguments why 3-terminal phototransistors could provide greater technological opportunities. First, because they are electronic switches, detection and processing can take place in the same circuit element in phototransistors. 12 The complexity of commercial applications (as defined by the number of vertical processing steps), therefore, has the potential to be reduced significantly when using phototransistors. Second, the responsivity of a phototransistor can be tuned through the voltage applied to the third (gate) terminal. This is a characteristic that has no analog in photodiodes. 13 Finally, optoelectronic logic gates can be fabricated from adjacent phototransistors. 12 Under appropriate biasing conditions, these logic gates can be designed to exhibit large changes in output voltage from small changes in incident optical power density. 13,14

One of the most significant drawbacks to phototransistors, however, is the complexity of the relationship between photocurrent (I_{ph}) and incident optical power density (P). Photocurrent in thin-film transistors (TFTs) is defined as the source-drain current (I_D) under illumination minus the sourcedrain current in the dark. Contributions to $I_{\rm ph}$ are broadly attributable to two processes: the so-called photovoltaic

effect 15-17 and the so-called photoconductive effect. The relative contributions of each mechanism to $I_{\rm ph}$ are strongly dependent on material/device design and biasing conditions. 19,20 The photovoltaic effect is manifest as a photoinduced change in threshold voltage (V_T) , and is, therefore, phenomenologically analogous to a photogating effect. It can lead to significant amplification, and external quantum efficiencies (EQEs) $\gg 100\%$. Similarly, negative EQEs are possible when the magnitude of the threshold voltage increases under illumination.¹³ The photovoltaic effect is commonly attributed to a buildup of minority charge carriers under the source electrode, 19,20 but can conceivably be dominated by other phenomena such as optically induced trapping and detrapping, similar to negative bias illumination stress.

The photoconductive effect is analogous to what is observed in photodiodes and solar cells, where direct charge generation contributes to current. 19 When operating in a photoconductive-dominated regime, a roughly linear relationship between $I_{\rm ph}$ and P is observed at low optical power densities,² as are moderate EQEs (<100%).¹³ At higher optical power densities, increased recombination can cause deviations from linearity. 25 Because the photoconductive effect is attributed to direct charge generation, only gate capacitance limits the response time in this regime, and it can hence be much faster¹²

Received: May 28, 2020 Accepted: June 25, 2020 Published: July 9, 2020





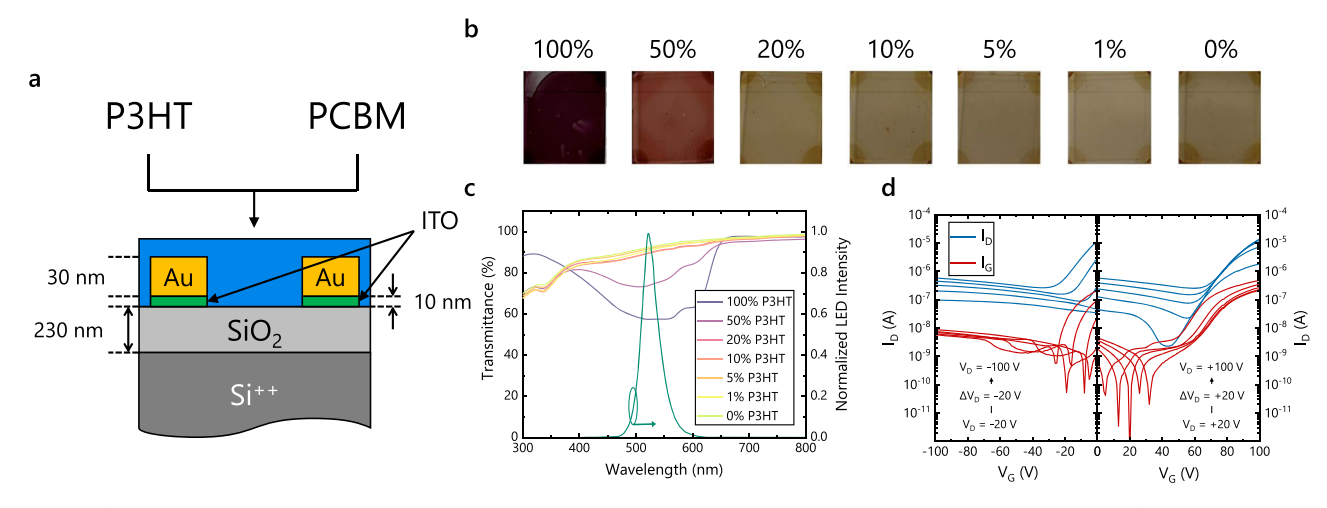


Figure 1. (a) Cross-sectional diagram of the BGBC architecture used in this study. Abbreviations are as follows, P3HT: poly(3-hexylthiophene-2,5-diyl), PCBM: phenyl- C_{61} -butyric acid methyl ester, Au: gold, ITO: indium tin oxide, SiO₂: silicon dioxide, and Si⁺⁺: highly doped (metallic) silicon. ITO acts as an adhesion layer for the gold source and drain electrodes. Si⁺⁺ acts as a substrate and global gate electrode. (b) Photographs of thin films of blends of P3HT and PCBM deposited onto quartz substrates, where percentage indicates the weight percentage of P3HT in the blend. (c) Transmittance (left) of thin films of blends of P3HT:PCBM in various ratios with normalized incident spectrum from the LED light source (right) used in this study.³⁵ (d) p-type (left) and n-type (right) transfer characteristics of the P3HT:PCBM (50:50) blend TFT measured in the dark. Source-drain current (I_D) is shown in blue and gate leakage current (I_G) is shown in red. The device has a channel length of 20 μm, a channel width of 1 cm, and a dielectric capacitance of 15 nF/cm². Each line is a measurement carried out at a different drain voltage (V_D) as indicated in the insets. Devices were measured under atmospheric pressure N₂ at room temperature.

than when operating in the photovoltaic regime, ²⁶ where the time-scales associated with trapping and detrapping dominate. ²⁷ Because of the faster response time, and relevance of the absorption properties of the semiconductor, operation in the photoconductive regime is in general desirable for most applications.

While both the photovoltaic and photoconductive effects occur in all phototransistors, their relative contribution can be controlled, to a certain extent, through a choice of gate voltage (V_G) . When the TFT is on $(|V_G| \gg |V_T|)$, small changes in V_T (photovoltaic effect) will lead to large changes in I_{D_t} overwhelming any contribution from the photoconductive effect. When the device is off ($|V_G| \ll |V_T|$), however, the channel is depleted and any directly generated charge should be easily detectable. When designing a device optimized for operation in the photoconductive regime, it is reasonable to expect the following criteria to be satisfied. (1) An effective means of generation and dissociation of charges must exist. While the applied gate voltage is expected to aid this process,²⁴ an interface such as a bulk-heterojunction 12 or bilayer 13 is likely to be required for effective dissociation in organic semiconductors. (2) Balanced charge transport pathways must exist for both electrons and holes. If these were not the case, one would expect a buildup of one species of charge, and hence a change in V_T . While ambipolar TFTs, ²⁹ such as those based on polymer:fullerene blends, ^{17,30} satisfy both these criteria, there are situations when one would prefer unipolar phototransistors, such as for complementary logic circuits with high gain.31

In this report, we study the relationship between the blending ratio and the device behavior in polymer:fullerene phototransistors. By adjusting the relative weight percentage of the p-type polymer poly(3-hexylthiophene-2,5-diyl) (P3HT) to the n-type small molecule phenyl- C_{61} -butyric acid methyl ester (PCBM), we are able to identify conditions giving rise to both unipolar electrical characteristics and an optimized photoresponse. Additionally, these devices exhibit a strong

photoresponse, even when the active layer is >90% transmitting to the relevant wavelength, demonstrating their potential use in fully transparent optical sensors.³²

■ EXPERIMENTAL SECTION

TFT Fabrication. Prepatterned bottom-gate, bottom-contact (BGBC) TFT substrates were purchased from Fraunhofer IPMS.³³ The devices employed a highly n-doped silicon ($\sim 10^{17}$ cm⁻³) as a global gate electrode, and a 230 nm thermally grown SiO₂ layer as a global gate dielectric. 30 nm thick gold source and drain contacts, with a 10 nm indium tin oxide (ITO) adhesion layer, were used as the source and drain contacts. Substrates were cleaned in acetone and isopropyl alcohol before semiconductor deposition. Two parent solutions, 20 mg/mL P3HT and 20 mg/mL PCBM, both in chlorobenzene, were made and left stirring overnight at 60 °C under atmospheric-pressure N2. Seven blended solutions were made from these parent solutions with 50, 20, 10, 5, 1, and 0% P3HT. Solutions were spin-cast onto the prepatterned TFT substrates at 1500 rpm for 1 min, and then annealed at 100 °C for 30 min in ambient-pressure N2 to drive off the solvent. P3HT was purchased from Sigma-Aldrich, it had an average molecular weight of 85,000-100,000 g/mol, and a regioregularity of ≥90%. PCBM was purchased from Solenne BV, and was >99.5% pure.

TFT Measurement. Two computer-controlled Keithley 2400 source meters were used to carry out electrical measurements. All devices were measured under ambient-pressure N_2 at room temperature using an Everbeing C-2 probe station. Mobility was extracted in the saturation regime using standard device models. A N-channel threshold voltage was estimated by extrapolating drain current (I_D) to zero in the linear regime. Phototransistor measurements were carried out using a ThorLabs SOLIS-525C high-power green light-emitting diode (LED) controlled with a ThorLabs DC2200 LED Controller.

Time-Resolved Microwave Conductivity. The time-resolved microwave conductivity (TRMC) system used in this study is as described in previous reports ^{36,37} but a brief description is provided here for completeness. Microwaves are generated using a Sivers IMA VO4280X/00 voltage-controlled oscillator (VCO). The signal has an approximate power of 16 dBm and a tunable frequency between 8 and 15 GHz. The VCO is powered with an NNS1512 TDK-Lambda

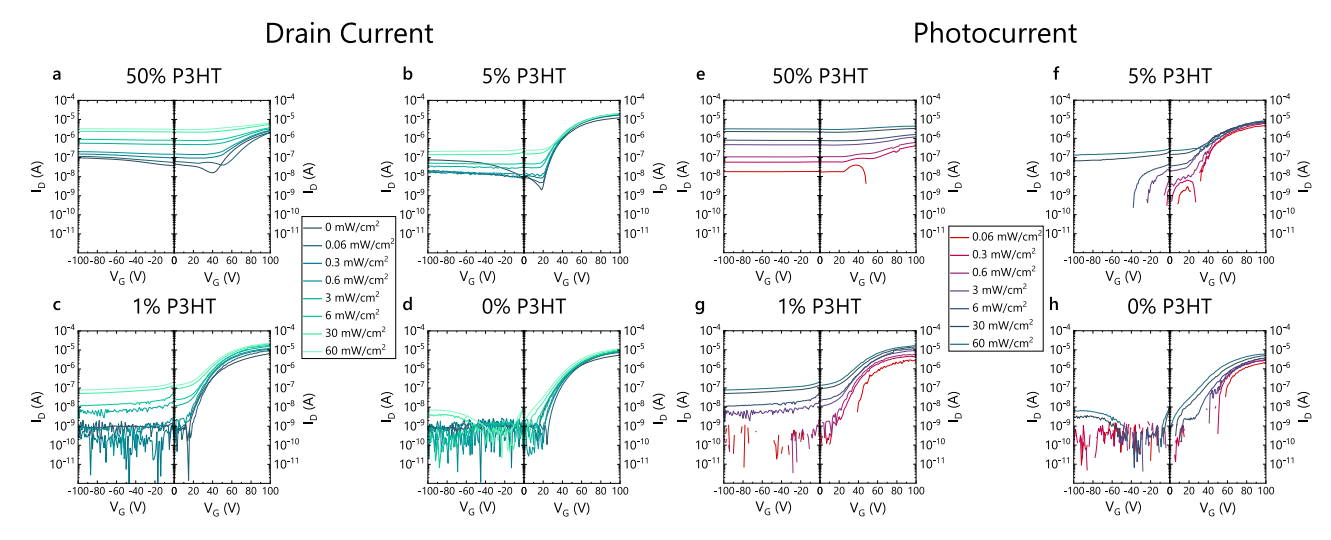


Figure 2. (a–d) Transfer characteristics (source-drain current, $I_{\rm D}$, as a function of gate voltage, $V_{\rm G}$) for TFTs formed of blends of P3HT and PCBM with various weight % of P3HT, measured under various intensities of green ($\lambda_{\rm max}$ = 525 nm) light. (e–h) Photocurrent ($I_{\rm ph}$ = $I_{\rm D}^{({\rm illuminated})}$ – $I_{\rm D}^{({\rm dark})}$) evaluated from the transfer characteristics shown in (a–d). Negative values of $I_{\rm ph}$ are not displayed.

constant 12 V power supply, and the output frequency is controlled using a Stahl Electronics BSA-Series voltage source. The oscillatory signal is incident on an antenna inside a WR90 copper-alloy waveguide. The incident microwaves pass through a fixed iris (6.35 mm diameter) into a sample cavity. The cavity supports a TE₁₀₃ mode standing wave and consists of an ITO-coated glass window that allows optical access to the sample. The sample is mounted inside the cavity at a maximum of the electric-field component of the standing microwaves, using a 3D-printed PLA sample holder. Microwaves reflected from the cavity are then incident on a zero bias Schottky diode detector (Fairview Microwave SMD0218). The detected voltage signal is amplified using a Femto HAS-X-1-40 high-speed amplifier (gain = ×100). The amplified detector voltage is measured as a function of time using a Textronix TDS 3032C digital oscilloscope. A Continuum Minilite II pulsed neodymium-doped yttrium aluminum garnet (Nd:YAG) laser is used to illuminate the sample. The laser pulse has a wavelength of 532 nm, a full width at half-maxima of approximately 5 ns, and a maximum fluence incident on the sample of $\sim 10^{15}$ photons/cm²/pulse. An external trigger link is employed to trigger the oscilloscope before the laser fires. The photoconductance and TRMC figure of merit $\phi \Sigma \mu$ were evaluated from changes in the detector voltage using standard analysis. 38,39 was measured as a function of fluence and fitted to a model⁴⁰ that accounts for biomolecular and Auger recombination in order to evaluate the representative value for sample each condition. All measurements were conducted in air, without encapsulation, in the overcoupled regime. Samples were prepared as described for TFT measurements, but on quartz substrates.

UV–Visible Spectroscopy. UV–visible absorption spectra were obtained using a Shimadzu UV–visible spectrometer UV-2600 ranging from 300 to 1000 nm for all samples.

■ RESULTS AND DISCUSSION

Figure 1a shows a cross-sectional diagram of the BGBC architecture used in this study. Note that this diagram is decidedly not to scale: the electrode separation was 20 μ m in all cases. Figure 1b shows the photographs of thin films of P3HT:PCBM on quartz, blended in various ratios. Figure 1c shows the corresponding optical transmittance of the films, along with the normalized LED emission spectrum. While the gate electrode and substrate are opaque, the transmittance data demonstrate that blend ratios of 20% or lower lead to highly transmitting films at the excitation wavelength. Figure 1d shows an example of transfer characteristics (I_D as a function of

 $V_{\rm G}$) for a 50:50 blend TFT in the dark. At this ratio, the device shows a characteristic ambipolar behavior.²⁹ Examples of dark transfer data for all other ratios studied are provided in Supporting Information Figure S1.

We illuminated the P3HT:PCBM blend phototransistors with green light ($\lambda_{\rm max}=525~{\rm nm}$) and measured the corresponding transfer characteristics in the p-type regime (negative $V_{\rm G}$) and the n-type regime (positive $V_{\rm G}$) at constant drain voltages of $V_{\rm D}=-20~{\rm V}$ and $V_{\rm D}=20~{\rm V}$, respectively. Because PCBM absorbs very little light at 525 nm, we expect that any changes in $I_{\rm D}$ as a result of illumination to be either due to charge generation in the P3HT, or trapping/detrapping effects. Figure 2a—d shows the transfer characteristics of four example P3HT:PCBM TFTs measured under illumination from green light with optical power densities between 60 μ W/cm² and 60 mW/cm². Similar data for other blend ratios are shown in Supporting Information Figure S2. At higher P3HT loadings, the transfer curves exhibit ambipolar behavior, 29 characterized by low-on off ratios. 31

All TFTs measured were in the BGBC architecture, as shown in Figure 1a. All devices had a channel length of 20 $\mu \rm m$, a channel width of 1 cm, and a dielectric capacitance of 15 nF/cm². Drain voltages of $V_{\rm D}=-20$ V were applied for negative $V_{\rm G}$ (left panels) and $V_{\rm D}=+20$ V were applied for positive $V_{\rm G}$ (right panels). All devices were measured under atmospheric pressure N_2 at room temperature. Legends show incident optical power density.

Figure 2e—h shows the photocurrent evaluated from Figure 2a—d. Photocurrent as a function of intensity is shown for all blend ratios in Supporting Information Figure S3. The fact that $I_{\rm ph}$ is negative (not shown) for certain conditions is indicative of a photo-induced shift in threshold voltage, associated with the photovoltaic effect. The 0% P3HT device shows very little change in off-current under illumination, which is not surprising given the very low absorption of PCBM at 525 nm (see Figure 1c). Importantly, however, Figure 2c,g reveals that even 1% of P3HT can have a significant effect on photoresponse. This result suggests using a very uneven blend ratio is a viable strategy to form unipolar, optically transparent phototransistors.

To further quantify the effect of the blend ratio, the responsivity (R) of the transistors can be evaluated, as defined using eq 1.

$$R = \frac{I_{\rm ph}}{\rm PLW} \tag{1}$$

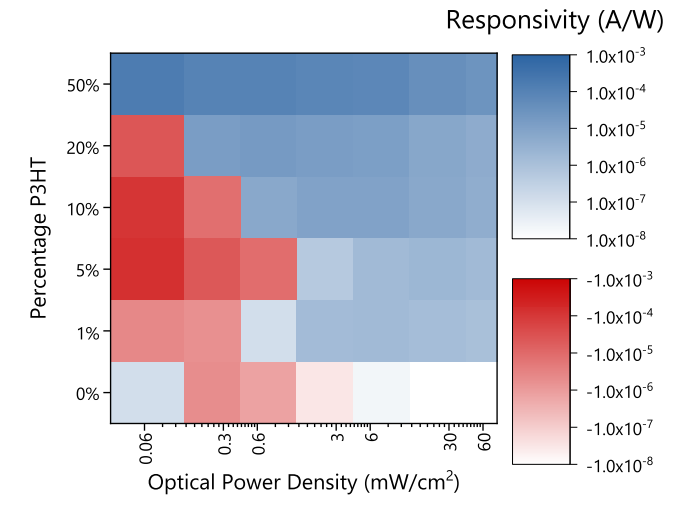
Here, P is the optical power density, L is the transistor channel length, and W is the transistor channel width. That is, the denominator is the total optical power incident in the transistor channel. Equation 1 is taken directly from the photodiode literature and care should be taken when interpreting values of R reported for phototransistors. According to widely used models for charge transport in TFTs, 34 $I_{\rm D}$ is linearly proportional to the ratio W/L. This means, one could significantly modify the drain current of a phototransistor by changing W/L, while keeping the product LW, and the denominator in eq 1, constant. While it has not been studied experimentally, it is likely that W/L, and hence $I_{\rm D}$ in the dark, will affect $I_{\rm ph}$. For this reason, care should be taken when comparing R between devices of different dimensions. In our study, however, we employ devices with $L=20~\mu{\rm m}$ and $W=1~{\rm cm}$ in all cases, enabling a direct comparison to be made.

Figure 3 shows responsivity extracted as a function of blend ratio and incident optical power density for applied voltages of a $V_{\rm D}=-20$ V, $V_{\rm G}=-20$ V and b $V_{\rm D}=20$ V, $V_{\rm G}=20$ V. We specifically choose combinations of gate and drain voltages where the TFT would be close to the off state, and hence $I_{\rm ph}$ is dominated by photoconductive behavior. Responsivity for applied gate voltages of $V_{\rm G}=\pm100$ V is shown in Supporting Information Figure S4 for comparison. The EQE is shown in Supporting Information Figure S5, where we observe all values to be $\ll 100\%$ at voltages of $V_{\rm G}$, $V_{\rm D}=\pm20$ V. Supporting Information Figure S6 shows the n-channel threshold voltage extracted as a function of blend ratio and optical power density and Supporting Information Figure S7 shows the ratio of photocurrent to dark drain current for voltages of $V_{\rm G}$, $V_{\rm D}=\pm20$ V.

When the device is operated in the p-type regime ($V_D = -20$ V, $V_G = -20$ V) we observe negative responsivities at low P3HT loadings and low P. While the dark I_D is relatively low under these conditions, the device is still on. For this reason, any small changes in the threshold voltage for either holes $(V_{\rm Th})$ or electrons $(V_{\rm Te})$ can shift the measured current at a particular combination of V_{D} and V_{G} to lower values. In the ntype regime ($V_{\rm D} = -20 \text{ V}$, $V_{\rm G} = -20 \text{ V}$), the device is held in a state close to being on, and hence most conditions give rise to a positive R. It is important to emphasize that the data in Figure 3 show only a snapshot of the relationship between responsivity and illumination because we have chosen a specific example of biasing conditions ($V_D = \pm 20 \text{ V}$, $V_G = \pm 20 \text{ V}$ V). Video S1 "S1.mp4" illustrates how large the parameter space is by sweeping from $V_G = 0 \text{ V}$ to $V_G = 100 \text{ V}$, at a fixed $V_{\rm D}$ = +20 V (a further dimension of parameter space is additionally available by changing V_D). The most important aspect of Figure 3 is the significant change in behavior observed as one goes from 0 to 1% P3HT loading. These data show how even a small amount of the photoactive component can enable desirable phototransistor properties.

To help gain a better understanding of the charge-generation processes in these blends, we carried out TRMC on P3HT:PCBM thin films on quartz. TRMC is a contactless technique, which enables one to evaluate photo-induced changes in conductance (ΔG) in response to above-band

a



b

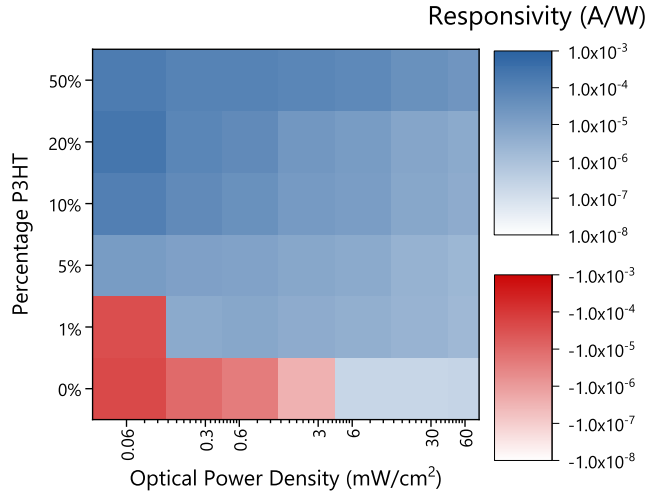


Figure 3. Responsivity of phototransistors formed of blends of P3HT and PCBM with various weight % of P3HT, measured under various intensities of green ($\lambda_{\rm max}=525$ nm) light, evaluated using eq 1. Responsivities were extracted with applied drain and gate voltages of a $V_{\rm D}=-20$ V and $V_{\rm G}=-20$ V, and b $V_{\rm D}=20$ V and $V_{\rm G}=20$ V, respectively. Blue represents positive responsivities and red represent negative responsivities. All phototransistors measured were in the BGBC architecture, as shown in Figure 1a, and had a channel length of 20 μ m, a channel width of 1 cm, and a dielectric capacitance of 15 nF/cm². All devices were measured under atmospheric pressure N₂ at room temperature.

gap optical stimulus (typically from a pulsed laser). 36,41,42 Because the technique is contactless, effects due to interfaces or injection (such as contact resistance) are avoided, but free charges do need to be generated and dissociated to be detected. Excitons are not detectable by TRMC. The conductance evaluated in TRMC is an area-average (illuminated part of the sample $\sim 1~{\rm cm}^2$) of local motion of charge carriers, moving in the plane of the sample. The charge carriers do not have to traverse a large region of the sample to go from electrode to electrode, as they do in TFTs. Figure 4a shows the TRMC transient data for four example thin films of P3HT:PCBM blends on quartz, with various blending ratios.

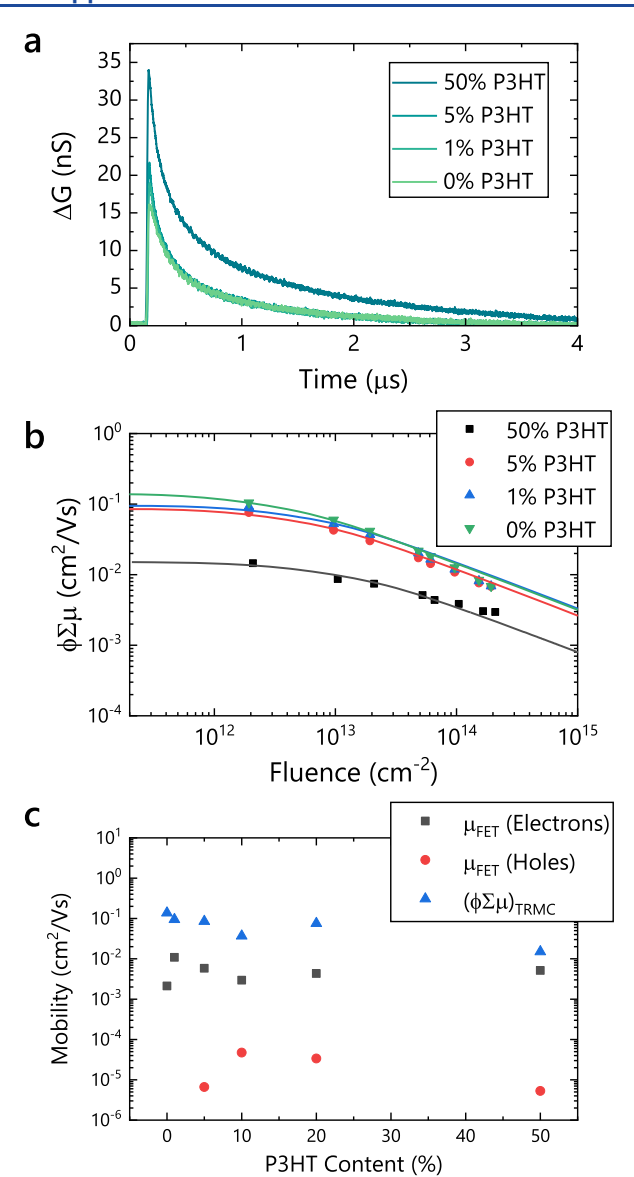


Figure 4. (a) Photo-induced change in conductance (ΔG) as a function of time before, during, and after illumination from a pulsed laser, for thin films of blended of P3HT and PCBM with various weight % of P3HT, on quartz substrates, evaluated using TRMC. The incident fluence was approximately 2 \times 10¹⁴ cm⁻² for all measurements shown. (b) TRMC figure of merit $(\phi \Sigma \mu)_{TRMC}$ = $\phi(\mu_e + \mu_h)$ for thin films of P3HT:PCBM blends with various weight % of P3HT, on quartz substrates, measured as a function of incident optical fluence. ϕ is the number of electron-hole pairs generated per absorbed photon, μ_e is the average electron mobility over the illuminated sample area, and μ_h is the average hole mobility over the illuminated sample area. The points are experimental values and the lines are fits to a numerical model⁴⁰ that accounts for bimolecular and Auger recombination during the laser pulse. (c) Field effect mobility (μ_{FET}) of electrons and holes evaluated from the thin-film-transistor (TFT) data in the dark, and $(\phi \Sigma \mu)_{\mathrm{TRMC}}$ evaluated from thin films on quartz, for P3HT:PCBM blends as a function of P3HT %. The laser had a wavelength of 532 nm, a temporal full width at half maximum of 5 ns for all TRMC measurements. All TRMC measurements were carried out in air at room temperature. All TFTs measured were in the BGBC architecture, as shown in Figure 1a and had a channel length of 20 μ m, a channel width of 1 cm, and a dielectric capacitance of 15 nF/cm². All TFTs were measured under atmospheric pressure N₂ at room temperature. TFT mobility was evaluated in the saturation regime using standard techniques.

Similar data for the other blending ratios are shown in Supporting Information Figure S8.

While the 50% P3HT film does show a larger signal than the other samples for roughly the same incident fluence, it is important to emphasize that the *y*-axis is simply conductance and is not normalized for the number of photons absorbed. In TRMC, it is more informative to evaluate the parameter $\phi \Sigma \mu$ from the photoconductance data, ⁴¹ as defined using eq 2.

$$\phi \sum \mu = \phi(\mu_{\rm e} + \mu_{\rm h}) \tag{2}$$

Here, ϕ is the number of electron-hole pairs generated per absorbed photon (between 0 and 1), μ_e is the average electron mobility over the illuminated sample area, and μ_h is the average hole mobility over the illuminated sample area. While $\phi \Sigma \mu$ has the same dimensions as charge carrier mobility, carrier-type specific information is obscured in the TRMC data. Nonetheless, its contactless nature makes it a valuable technique for evaluating the electronic properties of thin film semiconductors (in particular those studied for solar cells^{39,41,43–45}). Figure 4b shows $\phi \Sigma \mu$ measured as a function of laser fluence for the same four example thin films of P3HT:PCBM blends on quartz, with various blending ratios. Supporting Information Figure S9 shows the same data for all blends studied. The variation in $\phi \Sigma \mu$ with fluence is because of the increased bimolecular and Auger recombination occurring during the finite duration of the laser pulse, reducing the carrier concentration, and the observable $\phi \Sigma \mu$ below its expected value. A model developed to account for this phenomenon⁴⁰ has been applied to the data in Figure 4b, enabling us to extract a representative value of $\phi \Sigma \mu$ for each blend ratio. Figure 4c shows the representative values of $\phi \Sigma \mu$ plotted as a function of blend ratio, along with field effect mobility (μ_{FET}) extracted from the TFT data in the dark, for electrons and holes. P3HT:PCBM blends have been extensively studied with TRMC in the past, $^{46-49}$ and values of $\phi\Sigma\mu$ on the order of 10⁻⁴ to 10⁻² cm²/Vs are commonly observed.

While the electron field effect mobility is as expected for a P3HT:PCBM TFT,50 The hole mobility is significantly lower than expected for TFTs based on this polymer. 51 It is possible that the semiconductor-dielectric interface in this TFT is not optimized for P3HT⁵² or that hole percolation pathways⁵³ are disrupted by the PCBM.⁵⁴ It is worth noting that the sum of field effect mobilities for holes and electrons measured for the TFTs is lower than $\phi \Sigma \mu$ as evaluated by TRMC. Because TFTs probe charge transport over long distances, they require a continuous pathway over 20 μ m. Conversely, TRMC is a local probe. These differences could affect observable mobility in polymer:fullerene blends. For example, any dead-ends in the polymer-fullerene network would not be expected to contribute to current in TFTs,⁵⁰ but would still be valid locations for charge in TRMC measurements. While this difference is not expected to affect the trends observed in Figure 4c, it does make it impossible to directly evaluate ϕ from these data.

It is known that blend ratios close to 1:1 are required to achieve optimal power conversion efficiency in organic photovoltaics, ^{55–57} as larger PCBM concentrations lead to poor intermolecular packing of the polymer, ⁵⁵ and unbalanced percolation pathways. ⁵⁸ These are possible explanations for the low hole field effect mobility observed in our study. Furthermore, upon annealing, excessive clustering of PCBM has been observed ⁵⁹ leading to poor percolation pathways. ⁵⁰

Importantly, we observe that $\phi \Sigma \mu$ and μ_{FET} for electrons follow the same trend with the blending ratio. This suggests, at least for the P3HT content between 1 and 20%, that ϕ is not significantly affected by the blending ratio. At first glance, this may be unexpected, as one would assume the interfacial area between the two components to have a strong influence over exciton dissociation. However, it is important to remember that we are using a laser with a wavelength of 532 nm and are hence primarily exciting the P3HT. It has previously been shown that the polymer:fullerene interfacial area is maximized at 35% wt PCBM in P3HT:PCBM blends.60 Because all blending ratios in this present study involve ≥50% by weight PCBM, it is, therefore, likely that most P3HT regions of the film will be spatially close to some PCBM in most of the films studied. Consequently, we hypothesize that for the P3HT content from 1 to 20%, charge dissociation is not strongly dependent on the blending ratio, helping to explain why our low-P3HT content phototransistors respond surprisingly well to green light.

CONCLUSIONS

In summary, we have studied how the ratio of polymer to fullerene affects the performance of phototransistors formed of blended P3HT and PCBM. We find the surprising result that even a small percentage (1% by weight) of P3HT can modify the optical response of P3HT:PCBM blend phototransistors to green light significantly. Thin films of P3HT:PCBM on quartz were studied using the contactless characterization technique: TRMC. Combined, we used the carrier mobilities extracted from TRMC and transistor data to illustrate how carriergeneration efficiency is roughly independent of the blending ratio when P3HT \leq 20% by weight. Polymer:fullerene phototransistors such as those demonstrated in this report have the combined advantages of being highly optically transparent to the detectable wavelength, and exhibiting unipolar characteristics. These devices represent a significant step toward reliable opto-electronic logic gates, with high gain, and the potential for high optical transparency.

ASSOCIATED CONTENT

Supporting Information

The Supporting Information is available free of charge at https://pubs.acs.org/doi/10.1021/acsaelm.0c00445.

Dark transfer characteristics of all blend ratios; transfer characteristics under illumination for all blend ratios; photocurrent for all blend ratios; responsivity; EQE; photo-induced changes in n-channel threshold voltage; ratio of photocurrent to dark current; and TRMC data (PDF)

Responsivity measured as a function of gate voltage (MP4)

AUTHOR INFORMATION

Corresponding Author

John G. Labram — School of Electrical Engineering and Computer Science, Oregon State University, Corvallis, Oregon 97331, United States; ⊙ orcid.org/0000-0001-6562-9895; Email: john.labram@oregonstate.edu

Authors

Cinthya Trujillo Herrera — School of Electrical Engineering and Computer Science, Oregon State University, Corvallis, Oregon 97331, United States

Min Ji Hong — School of Electrical Engineering and Computer Science, Oregon State University, Corvallis, Oregon 97331, United States

Complete contact information is available at: https://pubs.acs.org/10.1021/acsaelm.0c00445

Notes

The authors declare no competing financial interest.

ACKNOWLEDGMENTS

The authors thank the National Science Foundation for financial support (award number: 1942558).

REFERENCES

- (1) Chang, J. S.; Facchetti, A. F.; Reuss, R. A Circuits and Systems Perspective of Organic/Printed Electronics: Review, Challenges, and Contemporary and Emerging Design Approaches. *IEEE Trans. Emerg. Sel. Topics Circuits Syst.* **2017**, 7, 7–26.
- (2) Street, R. A. Thin-Film Transistors. *Adv. Mater.* **2009**, *21*, 2007–2022.
- (3) Myny, K. The Development of Flexible Integrated Circuits Based on Thin-Film Transistors. *Nat. Electron.* **2018**, *1*, 30–39.
- (4) Sirringhaus, H. 25th Anniversary Article: Organic Field-Effect Transistors: The Path Beyond Amorphous Silicon. *Adv. Mater.* **2014**, 26, 1319–1335.
- (5) Yu, X.; Marks, T. J.; Facchetti, A. Metal Oxides for Optoelectronic Applications. *Nat. Mater.* **2016**, *15*, 383–396.
- (6) Lin, Y. H.; Pattanasattayavong, P.; Anthopoulos, T. D. Metal-Halide Perovskite Transistors for Printed Electronics: Challenges and Opportunities. *Adv. Mater.* **2017**, *29*, 1702838.
- (7) Gelinck, G.; Heremans, P.; Nomoto, K.; Anthopoulos, T. D. Organic Transistors in Optical Displays and Microelectronic Applications. *Adv. Mater.* **2010**, 22, 3778–3798.
- (8) Ng, T. N.; Wong, W. S.; Chabinyc, M. L.; Sambandan, S.; Street, R. A. Flexible Image Sensor Array with Bulk Heterojunction Organic Photodiode. *Appl. Phys. Lett.* **2008**, *92*, 213303.
- (9) Rauch, T.; Böberl, M.; Tedde, S. F.; Fürst, J.; Kovalenko, M. V.; Hesser, G.; Lemmer, U.; Heiss, W.; Hayden, O. Near-Infrared Imaging with Quantum-Dot-Sensitized Organic Photodiodes. *Nat. Photonics* **2009**, *3*, 332–336.
- (10) Jansen-van Vuuren, R. D.; Armin, A.; Pandey, A. K.; Burn, P. L.; Meredith, P. Organic Photodiodes: The Future of Full Color Detection and Image Sensing. *Adv. Mater.* **2016**, *28*, 4766–4802.
- (11) Simone, G.; Di Carlo Rasi, D.; de Vries, X.; Heintges, G. H. L.; Meskers, S. C. J.; Janssen, R. A. J.; Gelinck, G. H. Near-Infrared Tandem Organic Photodiodes for Future Application in Artificial Retinal Implants. *Adv. Mater.* **2018**, *30*, 1804678.
- (12) Anthopoulos, T. D. Electro-Optical Circuits Based on Light-Sensing Ambipolar Organic Field-Effect Transistors. *Appl. Phys. Lett.* **2007**, *91*, 113513.
- (13) Labram, J. G.; Wöbkenberg, P. H.; Bradley, D. D. C.; Anthopoulos, T. D. Low-Voltage Ambipolar Phototransistors Based on a Pentacene/ $PC_{61}BM$ Heterostructure and a Self-Assembled Nano-Dielectric. *Org. Electron.* **2010**, *11*, 1250–1254.
- (14) Lin, Y.-H.; Huang, W.; Pattanasattayavong, P.; Lim, J.; Li, R.; Sakai, N.; Panidi, J.; Hong, M. J.; Ma, C.; Wei, N.; Wehbe, N.; Fei, Z.; Heeney, M.; Labram, J. G.; Anthopoulos, T. D.; Snaith, H. J. Deciphering Photocarrier Dynamics for Tuneable High-Performance Perovskite-Organic Semiconductor Heterojunction Phototransistors. *Nat. Commun.* **2019**, *10*, 4475.
- (15) Choi, C.-S.; Kang, H.-S.; Woo-Young Choi, W.-Y.; Kim, H.-J.; Choi, W.-J.; Kim, D.-H.; Jang, K.-C.; Seo, K.-S. High Optical Responsivity of InAlAs-InGaAs Metamorphic High-Electron Mobility

- Transistor on GaAs Substrate with Composite Channels. *IEEE Photonics Technol. Lett.* **2003**, *15*, 846–848.
- (16) Noh, Y.-Y.; Kim, D.-Y.; Yase, K. Highly Sensitive Thin-Film Organic Phototransistors: Effect of Wavelength of Light Source on Device Performance. *J. Appl. Phys.* **2005**, *98*, 074505.
- (17) Marjanović, N.; Singh, Th. B.; Dennler, G.; Günes, S.; Neugebauer, H.; Sariciftci, N. S.; Schwödiauer, R.; Bauer, S. Photoresponse of Organic Field-Effect Transistors Based on Conjugated Polymer/Fullerene Blends. *Org. Electron.* **2006**, *7*, 188–194.
- (18) Singh, T. B.; Koeppe, R.; Sariciftci, N. S.; Morana, M.; Brabec, C. J. Monitoring the Channel Formation in Organic Field-Effect Transistors via Photoinduced Charge Transfer. *Adv. Funct. Mater.* **2009**, *19*, 789–795.
- (19) Baeg, K.-J.; Binda, M.; Natali, D.; Caironi, M.; Noh, Y.-Y. Organic Light Detectors: Photodiodes and Phototransistors. *Adv. Mater.* **2013**, *25*, 4267–4295.
- (20) Gu, P.; Yao, Y.; Feng, L.; Niu, S.; Dong, H. Recent Advances in Polymer Phototransistors. *Polym. Chem.* **2015**, *6*, 7933–7944.
- (21) Guo, Y.; Du, C.; Yu, G.; Di, C.-a.; Jiang, S.; Xi, H.; Zheng, J.; Yan, S.; Yu, C.; Hu, W.; Liu, Y. High-Performance Phototransistors Based on Organic Microribbons Prepared by a Solution Self-Assembly Process. *Adv. Funct. Mater.* **2010**, *20*, 1019–1024.
- (22) Pattanasattayavong, P.; Rossbauer, S.; Thomas, S.; Labram, J. G.; Snaith, H. J.; Anthopoulos, T. D. Solution-Processed Dye-Sensitized ZnO Phototransistors with Extremely High Photoresponsivity. *J. Appl. Phys.* **2012**, *112*, 074507.
- (23) Nomura, K.; Kamiya, T.; Hosono, H. Interface and bulk effects for bias-light-illumination instability in amorphous-In-Ga-Zn-O thin-film transistors. *J. Soc. Inf. Disp.* **2010**, *18*, 789–795.
- (24) Noh, Y.-Y.; Kim, D.-Y.; Yoshida, Y.; Yase, K.; Jung, B.-J.; Lim, E.; Shim, H.-K. High-Photosensitivity p-Channel Organic Phototransistors Based on a Biphenyl End-Capped Fused Bithiophene Oligomer. *Appl. Phys. Lett.* **2005**, *86*, 043501.
- (2S) Wasapinyokul, K.; Milne, W. I.; Chu, D. P. Photoresponse and Saturation Behavior of Organic Thin Film Transistors. *J. Appl. Phys.* **2009**, *105*, 024509.
- (26) Saragi, T. P. I.; Pudzich, R.; Fuhrmann, T.; Salbeck, J. Organic Phototransistor Based on Intramolecular Charge Transfer in a Bifunctional Spiro Compound. *Appl. Phys. Lett.* **2004**, *84*, 2334–2336.
- (27) Lopes, M. E.; Gomes, H. L.; Medeiros, M. C. R.; Barquinha, P.; Pereira, L.; Fortunato, E.; Martins, R.; Ferreira, I. Gate-Bias Stress in Amorphous Oxide Semiconductors Thin-Film Transistors. *Appl. Phys. Lett.* **2009**, *95*, 063502.
- (28) Lloyd-Hughes, J.; Richards, T.; Sirringhaus, H.; Johnston, M. B.; Herz, L. M. Exciton Dissociation in Polymer Field-Effect Transistors Studied Using Terahertz Spectroscopy. *Phys. Rev. B: Condens. Matter Mater. Phys.* **2008**, *77*, 125203.
- (29) Smits, E. C. P.; Anthopoulos, T. D.; Setayesh, S.; van Veenendaal, E.; Coehoorn, R.; Blom, P. W. M.; de Boer, B.; de Leeuw, D. M. Ambipolar Charge Transport in Organic Field-Effect Transistors. *Phys. Rev. B: Condens. Matter Mater. Phys.* **2006**, 73, 205316.
- (30) Hamilton, M. C.; Martin, S.; Kanicki, J. Thin-Film Organic Polymer Phototransistors. *IEEE Trans. Electron Devices* **2004**, *51*, 877–885.
- (31) Ford, M. J.; Labram, J. G.; Wang, M.; Wang, H.; Nguyen, T.-Q.; Bazan, G. C. Carrier-Selective Traps: A New Approach for Fabricating Circuit Elements with Ambipolar Organic Semiconductors. *Adv. Electron. Mater.* **2017**, *3*, 1600537.
- (32) Kim, B. J.; Cho, N.-K.; Park, S.; Jeong, S.; Jeon, D.; Kang, Y.; Kim, T.; Kim, Y. S.; Han, I. K.; Kang, S. J. Highly Transparent Phototransistor Based on Quantum-Dots and ZnO Bilayers for Optical Logic Gate Operation in Visible-Light. *RSC Adv.* **2020**, *10*, 16404–16414.
- (33) Organic Field Effect Transistors (OFET)—Fraunhofer IPMS. http://www.ipms.fraunhofer.de/en/research-development/end-of-line-test-substrates/ofet.html (accessed May 19, 2020).

- (34) Zaumseil, J.; Sirringhaus, H. Electron and Ambipolar Transport in Organic Field-Effect Transistors. *Chem. Rev.* **200**7, *107*, 1296–1323.
- (35) Thorlabs—SOLIS-525C High-Power LED for Microscopy, 525 nm (Green), 2.4 W (Min). https://www.thorlabs.com/thorproduct.cfm?partnumber=SOLIS-525C (accessed May 19, 2020).
- (36) Hong, M. J.; Svadlenak, S. R.; Goulas, K. A.; Labram, J. G. Thermal Stability of Mobility in Methylammonium Lead Iodide. *J. Phys. Mater.* **2019**, *3*, 014003.
- (37) Hong, M. J.; Johnson, R. Y.; Labram, J. G. Impact of Moisture on Mobility in Methylammonium Lead Iodide and Formamidinium Lead Iodide. *J. Phys. Chem. Lett.* **2020**, *11* (13), 4976–4983.
- (38) Savenije, T. J.; Ferguson, A. J.; Kopidakis, N.; Rumbles, G. Revealing the Dynamics of Charge Carriers in Polymer:Fullerene Blends Using Photoinduced Time-Resolved Microwave Conductivity. *J. Phys. Chem. C* **2013**, *117*, 24085–24103.
- (39) Labram, J. G.; Venkatesan, N. R.; Takacs, C. J.; Evans, H. A.; Perry, E. E.; Wudl, F.; Chabinyc, M. L. Charge transport in a two-dimensional hybrid metal halide thiocyanate compound. *J. Phys. Chem. C* **2017**, *5*, 5930–5938.
- (40) Labram, J. G.; Chabinyc, M. L. Recombination at High Carrier Density in Methylammonium Lead Iodide Studied Using Time-Resolved Microwave Conductivity. *J. Appl. Phys.* **2017**, *122*, 065501.
- (41) Savenije, T. J.; Ferguson, A. J.; Kopidakis, N.; Rumbles, G. Revealing the Dynamics of Charge Carriers in Polymer:Fullerene Blends Using Photoinduced Time-Resolved Microwave Conductivity. *J. Phys. Chem. C* **2013**, *117*, 24085–24103.
- (42) Reid, O. G.; Moore, D. T.; Li, Z.; Zhao, D.; Yan, Y.; Zhu, K.; Rumbles, G. Quantitative Analysis of Time-Resolved Microwave Conductivity Data. *J. Phys. D: Appl. Phys.* **2017**, *50*, 493002.
- (43) Oga, H.; Saeki, A.; Ogomi, Y.; Hayase, S.; Seki, S. Improved Understanding of the Electronic and Energetic Landscapes of Perovskite Solar Cells: High Local Charge Carrier Mobility, Reduced Recombination, and Extremely Shallow Traps. *J. Am. Chem. Soc.* **2014**, *136*, 13818–13825.
- (44) Semonin, O. E.; Elbaz, G. A.; Straus, D. B.; Hull, T. D.; Paley, D. W.; van der Zande, A. M.; Hone, J. C.; Kymissis, I.; Kagan, C. R.; Roy, X.; Owen, J. S. Limits of Carrier Diffusion in n -Type and p -Type CH 3 NH 3 PbI 3 Perovskite Single Crystals. *J. Phys. Chem. Lett.* **2016**, *7*, 3510–3518.
- (45) Hutter, E. M.; Gélvez-Rueda, M. C.; Bartesaghi, D.; Grozema, F. C.; Savenije, T. J. Band-Like Charge Transport in Cs2AgBiBr6 and Mixed Antimony–Bismuth Cs2AgBi_{1-X}Sb_xBr₆ Halide Double Perovskites. *ACS Omega* **2018**, *3*, 11655–11662.
- (46) Dicker, G.; de Haas, M. P.; Siebbeles, L. D. A.; Warman, J. M. Electrodeless Time-Resolved Microwave Conductivity Study of Charge-Carrier Photogeneration in Regioregular Poly(3-Hexylthiophene) Thin Films. *Phys. Rev. B: Condens. Matter Mater. Phys.* **2004**, 70, 045203.
- (47) Savenije, T. J.; Kroeze, J. E.; Yang, X.; Loos, J. The Formation of Crystalline P3HT Fibrils upon Annealing of a PCBM:P3HT Bulk Heterojunction. *Thin Solid Films* **2006**, *511–512*, 2–6.
- (48) Ferguson, A. J.; Kopidakis, N.; Shaheen, S. E.; Rumbles, G. Quenching of Excitons by Holes in Poly(3-Hexylthiophene) Films. *J. Phys. Chem. C* **2008**, *112*, 9865–9871.
- (49) Saeki, A.; Tsuji, M.; Seki, S. Direct Evaluation of Intrinsic Optoelectronic Performance of Organic Photovoltaic Cells with Minimizing Impurity and Degradation Effects. *Adv. Energy Mater.* **2011**, *1*, 661–669.
- (50) Labram, J. G.; Domingo, E. B.; Stingelin, N.; Bradley, D. D. C.; Anthopoulos, T. D. In-Situ Monitoring of the Solid-State Microstructure Evolution of Polymer:Fullerene Blend Films Using Field-Effect Transistors. *Adv. Funct. Mater.* **2011**, *21*, 356–363.
- (51) Sirringhaus, H.; Brown, P. J.; Friend, R. H.; Nielsen, M. M.; Bechgaard, K.; Langeveld-Voss, B. M. W.; Spiering, A. J. H.; Janssen, R. a. J.; Meijer, E. W.; Herwig, P.; de Leeuw, D. M. Two-Dimensional Charge Transport in Self-Organized, High-Mobility Conjugated Polymers. *Nature* 1999, 401, 685–688.

- (52) Chua, L.-L.; Zaumseil, J.; Chang, J.-F.; Ou, E. C.-W.; Ho, P. K.-H.; Sirringhaus, H.; Friend, R. H. General Observation of N-Type Field-Effect Behaviour in Organic Semiconductors. *Nature* **2005**, 434, 194–199.
- (53) Smith, J.; Heeney, M.; McCulloch, I.; Malik, J. N.; Stingelin, N.; Bradley, D. D. C.; Anthopoulos, T. D. Percolation Behaviour in High Mobility P-Channel Polymer/Small-Molecule Blend Organic Field-Effect Transistors. *Org. Electron.* **2011**, *12*, 143–147.
- (54) Mihailetchi, V. D.; Koster, L. J. A.; Blom, P. W. M.; Melzer, C.; de Boer, B.; van Duren, J. K. J.; Janssen, R. a. J. Compositional Dependence of the Performance of Poly(p-Phenylene Vinylene):Methanofullerene Bulk-Heterojunction Solar Cells. *Adv. Funct. Mater.* **2005**, *15*, 795–801.
- (55) Kim, Y.; Choulis, S. A.; Nelson, J.; Bradley, D. D. C.; Cook, S.; Durrant, J. R. Composition and Annealing Effects in Polythiophene/Fullerene Solar Cells. *J. Mater. Sci.* **2005**, *40*, 1371–1376.
- (56) Chirvase, D.; Parisi, J.; Hummelen, J. C.; Dyakonov, V. Influence of nanomorphology on the photovoltaic action of polymerfullerene composites. *Nanotechnology* **2004**, *15*, 1317–1323.
- (57) Brabec, C. J.; Heeney, M.; McCulloch, I.; Nelson, J. Influence of Blend Microstructure on Bulk Heterojunction Organic Photovoltaic Performance. *Chem. Soc. Rev.* **2011**, *40*, 1185–1199.
- (58) Lee, C.-K.; Pao, C.-W.; Chu, C.-W. Multiscale Molecular Simulations of the Nanoscale Morphologies of P3HT:PCBM Blends for Bulk Heterojunction Organic Photovoltaic Cells. *Energy Environ. Sci.* **2011**, *4*, 4124–4132.
- (59) Ma, W.; Yang, C.; Gong, X.; Lee, K.; Heeger, A. J. Thermally Stable, Efficient Polymer Solar Cells with Nanoscale Control of the Interpenetrating Network Morphology. *Adv. Funct. Mater.* **2005**, *15*, 1617–1622.
- (60) Müller, C.; Ferenczi, T. A. M.; Campoy-Quiles, M.; Frost, J. M.; Bradley, D. D. C.; Smith, P.; Stingelin-Stutzmann, N.; Nelson, J. Binary Organic Photovoltaic Blends: A Simple Rationale for Optimum Compositions. *Adv. Mater.* **2008**, *20*, 3510–3515.